Nano Research

Open Access

Research Article

Engineering frustrated Lewis pairs on graphitic carbon nitride for efficient photocatalytic degradation and detoxification of tetracycline

Yao Xiao[1,§], Liberty L. Mguni[2,§], Yashi Chen[1,§], Xiao Xu[1] ✉, Ziying Sun[1], Zhiyan He[1], Shan Wang[3], Sónia A.C. Carabineiro[4], Yali Yao[2], and Junjiang Zhu[1] ✉

[1] *Hubei Key Laboratory for Clean Recycling and Resource Utilization of Waste Fibers, College of Chemistry and Chemical Engineering, Wuhan Textile University, Wuhan 430200, China*
[2] *Institute for Catalysis and Energy Solution (ICES), College of Science, Engineering and Technology, University of South Africa (UNISA), Florida, Johannesburg 1710, South Africa*
[3] *College of Pharmacy, Dali University, Dali 671003, China*
[4] *LAQV-REQUIMTE, Department of Chemistry, NOVA School of Science and Technology, Universidade NOVA de Lisboa, 2829-516 Caparica, Portugal*
§ *Yao Xiao, Liberty L. Mguni, and Yashi Chen contributed equally to this work.*

Cite this article: *Nano Research*, **2026**, *19*, 94908399. https://doi.org/10.26599/NR.2026.94908399

ABSTRACT: Heterogeneous photocatalysis is a promising advanced oxidation process for the removal of organic pollutants, yet its efficiency is often limited by thermodynamic barriers and insufficient pollutant activation. Herein, we report the construction of frustrated Lewis pairs (FLPs) on graphitic carbon nitride (CN) to address these challenges and achieve enhanced photocatalytic degradation of tetracycline (TC). FLPs are introduced by an alkalization treatment, which introduces carbon vacancies (CVs) as Lewis acid (LA) sites and adjacent surface hydroxyl groups as Lewis base (LB) sites. This unique dual-sites configuration markedly improves charge separation, optimizes the band structure, and enhances the redox potential of CN. Furthermore, the synergistic "push–pull" electron effect of FLPs enables efficient activation of TC molecules, facilitating rapid oxidation by photogenerated holes. As a result, the optimized catalyst (CN-OH-15) achieves a degradation rate constant of 0.045 min^{-1}, nearly four times higher than pristine CN. Mechanistic studies reveal that the degradation pathway proceeds through demethylation, decarbonylation and ring-opening reactions, effectively reducing the toxicity of intermediates and creating a favorable basis for integration with biological treatment. This study demonstrates FLP engineering as a powerful strategy for pollutant activation and to regulate degradation pathways for sustainable wastewater remediation.

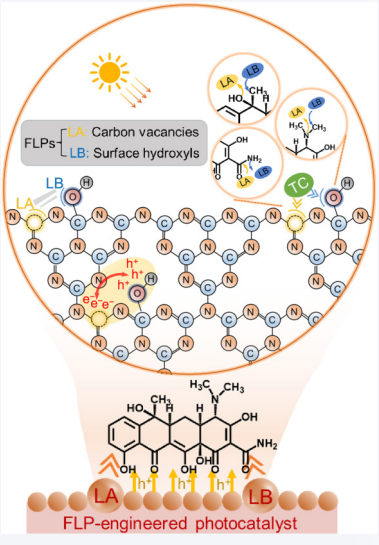

KEYWORDS: frustrated Lewis pairs, carbon vacancies, surface hydroxyl groups, pollutant activation, graphitic carbon nitride

1 Introduction

The rapid growth of global industry and agriculture has intensified environmental pollution, with organic contaminants emerging as one of the most pressing challenges for human and ecosystem health [1–4]. Among these, tetracycline (TC), a broad-spectrum antibiotic extensively used in medicine and animal husbandry, has drawn particular concern due to its widespread overuse and misuse [5]. Over 70% of administered TC is excreted in its unmetabolized form, resulting in its direct release into aquatic environments, where it poses significant ecological and public health risks [6, 7]. Its high stability and resistance to conventional treatments further contribute to its persistence in the environment [8].

Photocatalysis has emerged as one of the most promising

Received: November 26, 2025; **Revised:** December 22, 2025
Accepted: January 1, 2026

✉Address correspondence to Xiao Xu, xxu@wtu.edu.cn; Junjiang Zhu, jjzhu@wtu.edu.cn

advanced oxidation processes (AOPs) for pollutant degradation [9, 10]. A key challenge in the photocatalytic degradation is overcoming the intrinsic molecular stability of pollutants and lowering the high thermodynamic barrier for ring-opening reactions [11]. To improve pollutant activation, constructing electron-localized active sites has been widely explored [12–15]. For example, Yang et al. demonstrated that introducing oxygen vacancies into ultrathin Bi_2WO_6 creates localized electrons, which improved the electron transfer from the catalyst to pollutants [16]. Nevertheless, such single-site strategies only enable unidirectional electron transfer, leading to electron accumulation and limited polarization efficacy. In contrast, a bidirectional electron bridge facilitates efficient electron exchange and induces stronger polarization. Therefore, the design of dual sites capable of exerting a synergistic "push–pull" electron effect has emerged as a promising strategy to overcome the limitations of single-site systems and achieve enhanced pollutant activation [17–19].

In recent years, frustrated Lewis pairs (FLPs) have attracted significant attention in photocatalysis [20]. Unlike single electron-donating sites, FLPs feature dual active sites: Lewis acid (LA) and Lewis base (LB), that establish a cooperative microenvironment. This configuration prevents conventional adduct formation while enabling synergistic activation of target molecules [21, 22]. Defect engineering with precise spatial control has proven to be an effective strategy for constructing FLPs, as demonstrated in semiconductor photocatalysts, such as CeO_2, TiO_2, and Bi_2WO_6 [23–25]. Typically, the distance from defect sites (acting as LA) to adjacent surface hydroxyl groups (serving as LB) is 3–5 Å [26, 27]. Such an arrangement suppresses stable LA-LB adducts and simultaneously creates a highly reactive microenvironment [28]. As a result, FLPs exhibit exceptional capability in activating small molecules, such as H_2, CO_2, and H_2O, thereby promoting their efficient conversion in photocatalytic processes [29, 30].

Graphitic carbon nitride (CN), a metal-free semiconductor, has gained great attention in photocatalysis owing to its chemical stability, tunable electronic structure, and visible-light activity [31]. Conventional CN suffers from insufficient active sites and rapid charge recombination, which critically limit its photocatalytic efficiency in wastewater treatment [32]. FLPs present a promising strategy to address these limitations. Their unique "push–pull" electron configuration enables synergistic substrate activation, overcoming the inherent deficiencies of CN [33, 34]. For example, Yu et al. constructed FLPs on CN using B and N as Lewis acid-base sites, respectively, significantly enhancing O_2 and enhanced ethanol activation [35]. Inspired by the great success of FLPs in small molecule activation, extending this strategy to complex organic pollutants in water represents a promising advancement. However, the underlying reaction mechanism remains largely unexplored.

In this work, we successfully constructed FLPs on CN to enhance pollutant activation. FLPs were developed via a simple alkalization treatment, with carbon vacancies serving as Lewis acid sites and adjacent surface hydroxyl groups serving as Lewis base sites. The electronic and spatial configurations of FLPs were carefully examined and confirmed for facilitating the separation of photogenerated electron-hole pairs while promoting the activation of TC. The synergistic "push–pull" electron interaction between the FLPs and TC molecules accelerated interfacial electron transfer and enhanced molecular polarization (Scheme 1). As a result, the FLP-engineered CN achieved an impressive TC degradation rate of 0.045 min^{-1} while steering the degradation pathway toward reduced toxicity. This research establishes a generalizable strategy for designing high-performance photocatalytic systems by leveraging the "push–pull" electron effect of FLPs, providing an effective solution for enhanced pollutant activation in wastewater treatment.

2 Experimental

2.1 Sample preparation

All chemicals were of analytical grade and were used without further purification. Bulk carbon nitride was synthesized by thermal polymerizing 20 g of melamine in a muffle furnace, heating to 550 °C for 4 h. The resulting sample was denoted as CN. FLP-engineered CN was obtained through alkalization treatment. Briefly, 0.5 g of CN was dispersed in 60 mL of aqueous NaOH solutions with final concentrations of 0.17, 0.25, and 0.33 mol/L (prepared by adding 10, 15, and 20 mL of a 1.0 mol/L NaOH stock solution, respectively). The suspension was subjected to hydrothermal treatment at 160 °C for 12 h in a Teflon-lined autoclave. The resulting solid was collected by centrifugation, successively washed with deionized water, and vacuum-dried at 60 °C. The FLP-engineered samples were labeled CN-OH-10, CN-OH-15, and CN-OH-20 according to the volume of NaOH stock solution incorporated. For comparison, the control sample was prepared under identical hydrothermal conditions using deionized water instead of NaOH and designated as CN-H_2O.

2.2 Analytical methods

X-ray diffraction (XRD) patterns were collected on a Rigaku Ultima IV diffractometer using Cu Kα radiation (λ = 0.15418 nm).

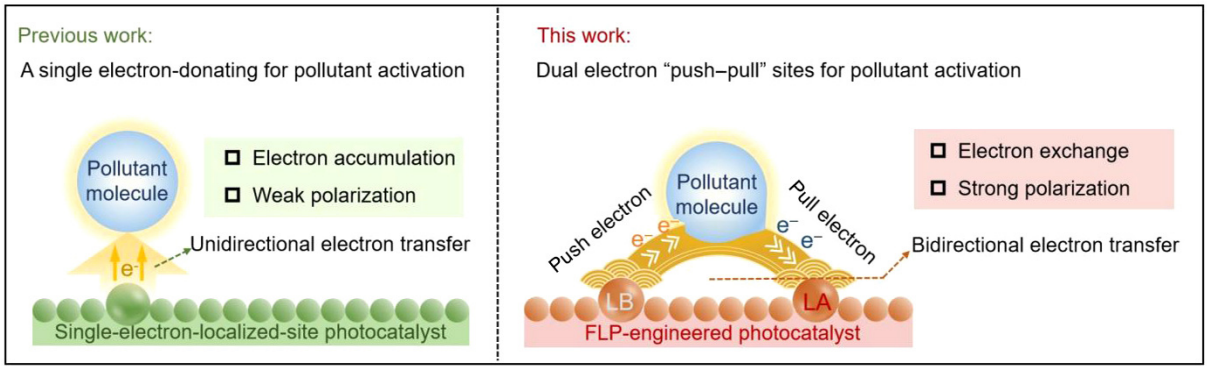

Scheme 1 Strategy for pollutant activation via constructing electron-localized sites. Previous work: A single electron-donating site for pollutant activation. This work: FLPs acting as dual sites to "push–pull" electron for pollutant activation.

Transmission electron microscopy (TEM) images were obtained with a JEOL JEM-NEOARM microscope. X-ray photoelectron spectroscopy (XPS) was performed on a Kratos XSAM800 system, with the C 1s peak at 284.6 eV used for energy calibration. Electron paramagnetic resonance (EPR) spectra were recorded at room temperature on a Magnettech MS-5000. Fourier transform infrared spectroscopy (FT-IR) spectra were measured on a Bruker TNESOR-27. Brunauer–Emmett–Teller (BET) specific surface area was determined using N_2 adsorption–desorption isotherms measured on a Beishide 3H-2000PS2 Surface Area and Pore Size Analyzer. Time-resolved photoluminescence (TRPL) decay spectra were collected on an Edinburgh Instruments FLS 1000 spectrometer under 375 nm excitation. Ultraviolet–visible-diffuse reflectance spectroscopy (UV–vis DRS) was performed on a Shimadzu UV-2600i spectrophotometer using $BaSO_4$ as the reference. Photocurrent response (PCR) and electrochemical impedance spectroscopy (EIS) were measured on a CHI 660D electrochemical workstation. *In-situ* Raman spectra were acquired on a Horiba Xplora Plus spectrometer with a 785 nm laser under simultaneous light irradiation introduced through the instrument's optical window. Zeta potentials were measured on a Malvern zetasizer (Nano ZS) analyzer. Reactive oxygen species (ROS) were detected by EPR spectroscopy using spin-trapping agents: 5,5-dimethyl-1-pyrroline-N-oxide (DMPO) for ·OH and $\cdot O_2^-$ and 2,2,6,6-tetramethylpiperidine (TEMP) for $^1O_2$ in aqueous solution.

2.3 Density functional theory (DFT) calculations

The spatial separation between the Lewis acid and base sites was determined through the DFT, as implemented by Vienna *ab initio* simulation package (VASP). The exchange-correlation energy was treated by Perdew–Burke–Ernzerhof (PBE) functional based on the generalized-gradient approximation. The reciprocal space integration was approximated with a Monkhorst–Pack *k*-point grid of 3 × 3 × 1 for all calculations. The convergence criterion for self-consistent iteration was set to 1×10^{-5} eV/atom and fully relaxed the systems until the final force on each atom was less than 0.02 eV/Å.

2.4 Photocatalytic activity tests

The photocatalytic activity was evaluated though the degradation of TC under visible light irradiation ($\lambda > 420$ nm). In a typical experiment, 50 mg of catalyst was dispersed in 50 mL of TC solution (20 mg/L) within a photocatalytic reactor. The suspension was stirred in the dark for 30 min to reach adsorption–desorption equilibrium, after which a Xenon lamp was switched to initiate the reaction. Aliquots (2 mL) were withdrawn at 10 min intervals, filtered and analyzed. The concentrations of TC and organic pollutants were determined using high-performance liquid chromatograph (HPLC, SPD-20A, Shimadzu) and detection wavelengths of 360 nm (TC), 275 nm (ciprofloxacin (CIP)), and 270 nm (sulfathiazole (ST)).

The degradation efficiency (η) of organic pollutants was calculated using the formula

$$\eta(\%) = (1 - C/C_0) \times 100 \quad (1)$$

where C_0 and C represent the initial concentration and the concentration at a given time, respectively.

The cycling stability of the catalyst was evaluated over four consecutive runs under identical experimental conditions. After each cycle, the used catalyst was collected, thoroughly washed with deionized water, vacuum-dried at 60 °C, and reused in the subsequent test.

2.5 *In-situ* diffuse reflectance infrared Fourier transform spectra (DRIFTS) experiments

To elucidate the role of FLPs in TC activation and photocatalytic degradation, *in-situ* DRIFTS was conducted on a Thermo Fisher Nicolet iS50 spectrometer equipped with a reaction cell and a liquid nitrogen-cooled mercury cadmium telluride (MCT) detector. A homogeneous mixture of CN-OH-15 (0.1 g) and TC (0.01 g) was ground for 15 min to ensure intimate interfacial contact and uniformly spread on the substrate in the reaction cell. Prior to measurements, the system was purged with argon (50 mL/min) at 150 °C for 1 h to remove surface contaminants. The photocatalytic reaction was then initiated under a continuous flow of air (30 mL/min) containing trace water vapor, while the MCT detector collected real-time infrared spectra with high sensitivity, enabling molecular-level monitoring of the degradation.

2.6 Intermediates analysis

The degradation intermediates of TC were analyzed using HPLC-mass spectrometry (HPLC-MS, Shimadzu 2020, Japan). Separation was carried out on a VP-ODS C18 reverse-phase column (5 μm, 15 × 4.6 mm) maintained at 30 °C. The mobile phase, delivered at 0.2 mL/min, consisted of solvent A (ultrapure water with 0.1% formic acid) and solvent B (acetonitrile). The injection volume was 20 μL. Mass spectrometric detection was performed in positive electrospray ionization (ESI^+) mode under the following optimized conditions: a capillary voltage of 4 kV, dry gas temperature of 350 °C, nebulizer voltage of 135 V, and nitrogen drying gas flow of 10 L/min. Spectra were recorded over a range of 100–500 *m*/*z*. Data were processed using the qualitative analysis module of Mass Hunter software for comprehensive identification of degradation intermediates.

2.7 Toxicological calculations

The toxicity of TC and its degradation intermediates was evaluated using the Ecological Structure Activity Relationships (ECOSAR program, version 2.0) and the Toxicity Estimation Software Tool (T.E.S.T.), both developed by the U.S. Environmental Protection Agency. These programs estimate the toxicity of organic compounds through quantitative structure–activity relationship (QSAR) modeling based on large chemical toxicity databases for structurally analogous compounds [36, 37]. The chronic toxicity was assessed by calculating the 48 h LC_{50} values for *Daphnia magna*. Developmental toxicity and mutagenicity were further evaluated using group contribution methods embedded in the software.

3 Results and discussion

3.1 Structural characterization and FLP formation mechanism

Figure 1(a) schematically illustrates the approach of constructing FLPs on CN via alkalization. The process creates a hydroxyl-rich and corrosive environment that simultaneously generates surface vacancies and hydroxyls on CN. The spatial proximity between these vacancies and hydroxyls establishes an ideal configuration for FLPs formation. The resulting FLPs induce a highly localized, electron-deficient environment on the CN surface, which significantly enhances the activation of reactant molecules during photocatalytic processes. The XRD patterns of CN before and after hydrothermal and alkalization (Fig. S1 in the Electronic

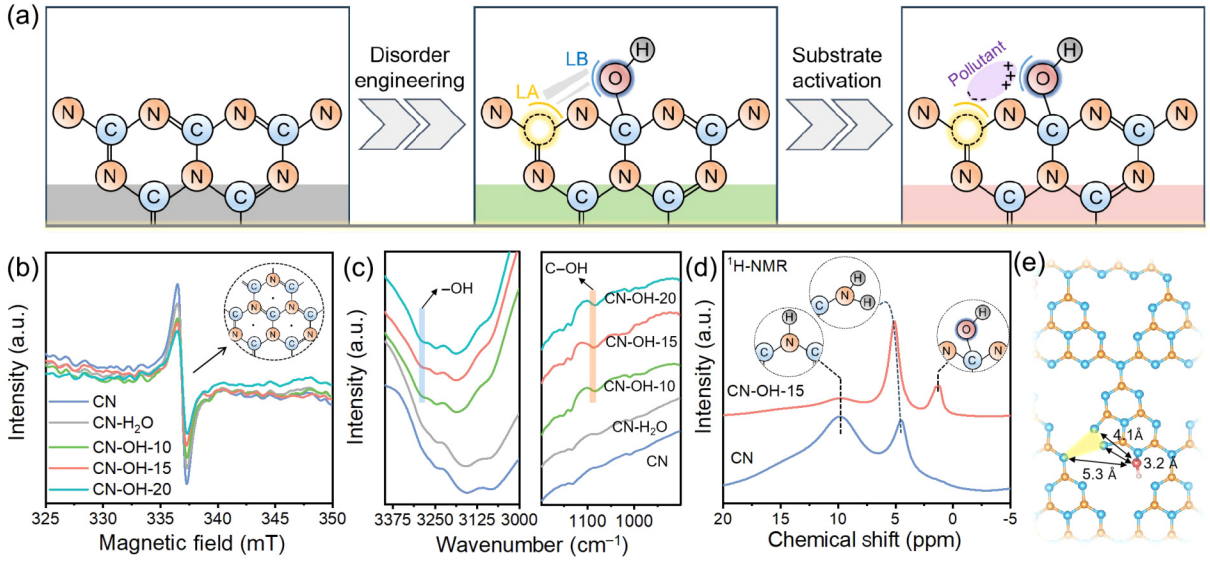

Figure 1 Structural characterization and FLP formation mechanism. (a) Schematic illustration of FLPs formation and pollutant activation. (b) EPR spectra. (c) FT-IR spectra and (d) ^{1}H ssNMR spectra of samples. (e) Spatial separation between LA and LB in CN-OH-15.

Supplementary Material (ESM)) showed negligible changes, confirming that the bulk crystalline structure remained largely intact. To probe the electronic modifications introduced by alkalization, EPR analysis was performed (Fig. 1(b)). All samples exhibited a characteristic signal at g = 2.001, corresponding to unpaired electrons in the heptazine units of CN [38]. Notably, the signal intensity decreased progressively with alkalization, which can be attributed to the formation of carbon vacancies (CVs) within the CN framework. This suggests that the alkaline environment selectively hydrolyzes of CN, thereby inducing CVs in a concentration-dependent manner.

FT-IR spectra displayed the characteristic vibrational modes of CN, including triazine ring bending (810 cm^{-1}), aromatic heterocycle stretching (1200–1600 cm^{-1}), and hydroxyl/amine group stretching (2900–3500 cm^{-1}) (Fig. S2 in the ESM). Notably, alkali-treated samples exhibited two additional peaks at 3289 and 1086 cm^{-1}, corresponding to surface hydroxyl and C–OH vibrations, respectively (Fig. 1(c)) [13]. XPS analysis of the O 1s region confirmed these findings, with CN-OH-15 vibrations exhibiting an extra peak at 533.2 eV, unambiguously assigned to C–O–H groups, which was absent in CN and CN-H_2O (Fig. S3 in the ESM). The spectra of ^{1}H solid-state nuclear magnetic resonance (ssNMR) (Fig. 1(d)) displayed characteristic peaks at 5.07 and 9.9 ppm, assigned to primary and secondary amines, respectively. For CN-OH-15, the primary amine resonance shifted downfield to 4.47 ppm, suggesting weakened interlayer van der Waals interactions and the formation of thinner nanosheets. In addition, a new peak at 1.28 ppm was observed in CN-OH-15, providing direct evidence for the introduction of surface hydroxyls (C–OH) through alkalization. Importantly, theoretical calculations confirmed that the spatial separation between surface hydroxyl groups and carbon vacancies, estimated to be 3.2–5.3 Å (Fig. 1(e)), falls within the optimal range for FLPs formation.

TEM reveals the morphological evolution of CN following alkalization (Fig. S4 in the ESM). While all samples maintained the characteristic layered structure of CN, significant differences were observed. Pristine CN consisted of thick, densely stacked aggregated, whereas CN-OH-15 transformed into ultrathin nanosheets due to combined alkaline etching and exfoliation. This structural rearrangement led to a remarkable increase in specific surface area, from 11.0 m^2/g for pristine CN to 115.6 m^2/g for CN-OH-15 (Fig. S5 and Table S1 in the ESM). Such morphological refinement and surface area enlargement greatly enhance the exposure of active sites and strengthen interfacial contact between the photocatalyst and pollutant molecules, thereby favoring photocatalytic reactions.

3.2 Photophysical and electrochemical characterization

The degree of alkalinization dictates the morphological dimensions, carbon vacancy concentration, and surface hydroxyl density of CN, thereby regulating the optical properties and band structure. As shown in Fig. 2(a), pristine CN exhibited a characteristic UV absorption edge near 470 nm, whereas the CN-OH-x series (x = 10, 15, 20) displayed blue-shifted absorption edges. This shift can be attributed to quantum confinement effects, arising from the transformation of bulk CN into thinner nanostructures under alkalinization. Among the samples, CN-OH-15 showed a distinctly enlarged band gap of 2.73 eV, compared to 2.66 eV for pristine CN (Fig. S6 in the ESM). The enlarged band gap, arising from nanoscale structural refinement, is expected to yield an enhanced redox potential, thereby improving suitability for photocatalytic applications.

To elucidate the role of FLPs in modulating charge carrier dynamics, we combined photoelectrochemical measurements with advanced spectroscopic analyses. CN-H_2O exhibited a lower photocurrent density than pristine CN (Fig. 2(b)), due to the suppression of charge separation by the more ordered interfaces formed during hydrothermal treatment. In contrast, FLP-engineered CN samples displayed markedly enhanced photocurrent responses, confirming that FLPs function as interfacial "relay stations" to facilitate charge separation. FLP-engineered samples, particularly CN-OH-15, exhibited smaller semicircle radii in Nyquist plots, indicative of reduced interfacial charge transfer resistance and improved charge mobility (Fig. 2(c)). Time-resolved PL decay analysis further validated this effect. CN-OH-15 exhibited a prolonged charge carrier lifetime of 3.08 ns, significantly longer than 2.19 ns of pristine CN (Fig. 2(d)). Together, these results demonstrate that FLP engineering enables CN with superior charge separation and migration.

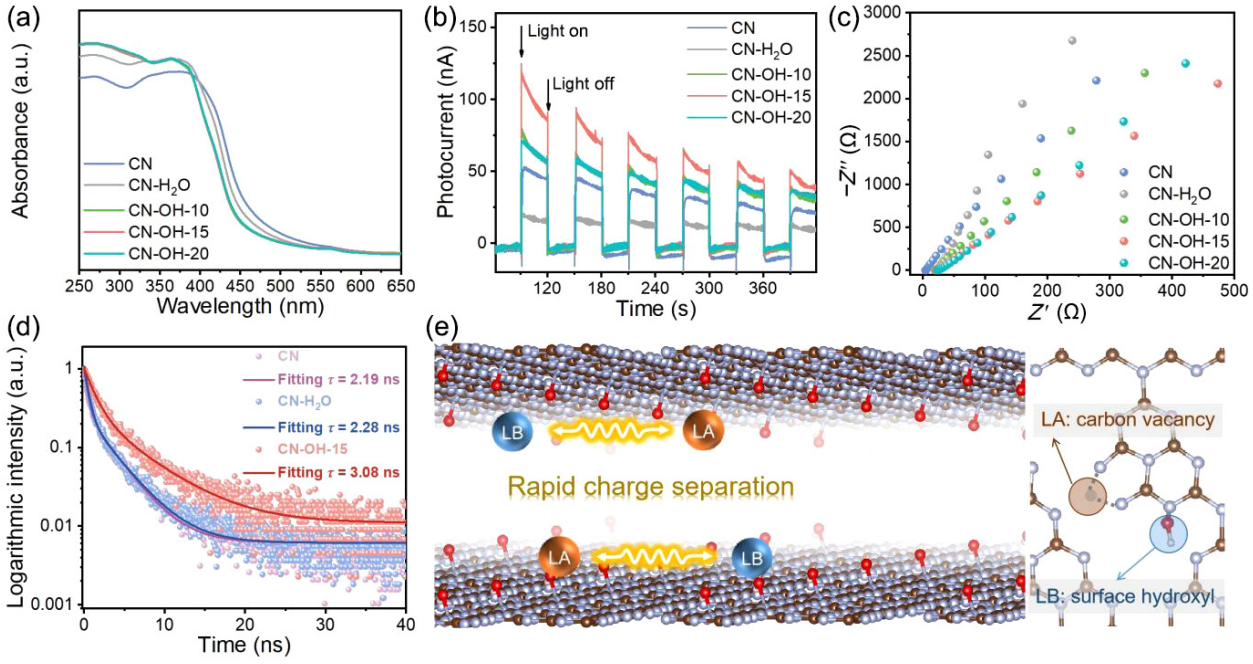

Figure 2 Photophysical and electrochemical characterization. (a) UV–vis absorption spectra. (b) Photocurrent response. (c) EIS Nyquist plots. (d) Time-resolved PL decay profiles. (e) Schematic illustration of FLP-mediated charge separation and migration via synergistic Lewis acid-base sites.

These results establish a positive correlation between FLP engineering and enhanced charge carrier dynamics. As illustrated in Fig. 2(e), the FLPs consist of CVs and adjacent surface hydroxyl groups. The CVs act as LA sites with vacant orbitals capable of capturing photogenerated electrons, while the hydroxyl groups serve as LB sites with filled orbitals that preferentially accumulate photogenerated holes. Upon photoexcitation, the synergistic cooperation between these complementary LA and LB sites provides an efficient charge separation pathway, enabling directional migration of free charge carriers. This dual-site activation mechanism not only strengthens intralayer electron transfer within CN-OH-15 but also promotes interlayer spatial charge migration, thereby advancing photocatalytic efficiency.

3.3 Photocatalytic performance evaluation

The photocatalytic performance evaluation revealed that CN-OH-15 achieved 87% TC degradation within 60 min, far exceeding the 52% removal observed for CN (Fig. 3(a)). Kinetic analysis confirmed that CN-OH-15 exhibited a remarkable rate constant of 0.045 min^{-1}, representing a 4.1-fold enhancement, compared to CN (0.011 min^{-1}) (Fig. S7 in the ESM). This pronounced improvement highlights the crucial role of FLPs in enhancing photocatalytic efficiency. To assess the practical applicability, the system was tested under simulated wastewater conditions. The introduction of common inorganic ions (Mg^{2+}, Ca^{2+}, NO_3^-, Cl^-, HCO_3^-) had little effect on the TC degradation efficiency over CN-OH-15 (Fig. 3(b) and Fig. S8 in the ESM). The slight decrease observed with HCO_3^- was attributed to pH variations during the reaction. Furthermore, CN-OH-15 maintained more than 85% TC removal efficiency within 60 min across diverse real water matrices (Fig. 3(c)). The maintained high performance in complex real water matrices suggests that the FLPs on CN-OH-15 have a strong and specific affinity for activating and adsorbing TC molecules. This interaction likely outcompetes the potential interference or scavenging effects from background organic matter and ions present in tap, lake, and river water, underscoring its potential for practical application. Beyond TC, CN-OH-15 also exhibited strong versatility, achieving efficient degradation over a range of functional group-rich organic contaminants (Fig. S9 in the ESM). Importantly, CN-OH-15 exhibited excellent stability, retaining consistent performance across four consecutive photocatalytic cycles without significant loss of activity (Fig. 3(d)). The excellent structural stability of CN-OH-15 was confirmed by the negligible changes observed in both XRD patterns and FT-IR spectra after multiple recycling tests (Figs. S10 and S11 in the ESM).

3.4 Effect of FLPs on TC degradation

To elucidate the specific role of FLPs in promoting TC degradation, we conducted systematic control experiments by thermally treating CN-OH-15 at 350 °C to disrupt the FLP structure (Fig. 4(a)). FT-IR analysis confirmed the complete removal of surface hydroxyl groups after calcination (Fig. S12 in the ESM). The FLP-disrupted CN-OH-15 exhibited markedly reduced photocatalytic activity, with the rate constant decreasing to 0.027 min^{-1}, significantly lower than that of intact CN-OH-15 (0.045 min^{-1}) (inset of Fig. 4(a)). This performance decline underscores that both LA (CVs) and LB (surface –OH) sites are indispensable and must act jointly to sustain the high catalytic efficiency. The involvement of reactive species was investigated by quenching experiments (Fig. 4(b)). The pronounced inhibition effect of triethanolamine (TEOA) suggested the dominant role of photogenerated holes (h^+) in TC degradation. In contrast, isopropanol (IPA) and β-carotene produced moderate inhibition, indicating that hydroxyl radicals (·OH) and singlet oxygen ($^1O_2$) contributed to a lesser extent. Superoxide dismutase (SOD) exhibited negligible influence, suggesting that superoxide radicals ($\cdot O_2^-$) were not significantly involved. These findings were corroborated by ROS detection, which revealed only weak signals for ·OH, $^1O_2$, and $\cdot O_2^-$ under light illumination (Fig. 4(c)). Collectively, these results indicate that CN-OH-15 primarily followed a hole-mediated pathway. In comparison, CN followed a

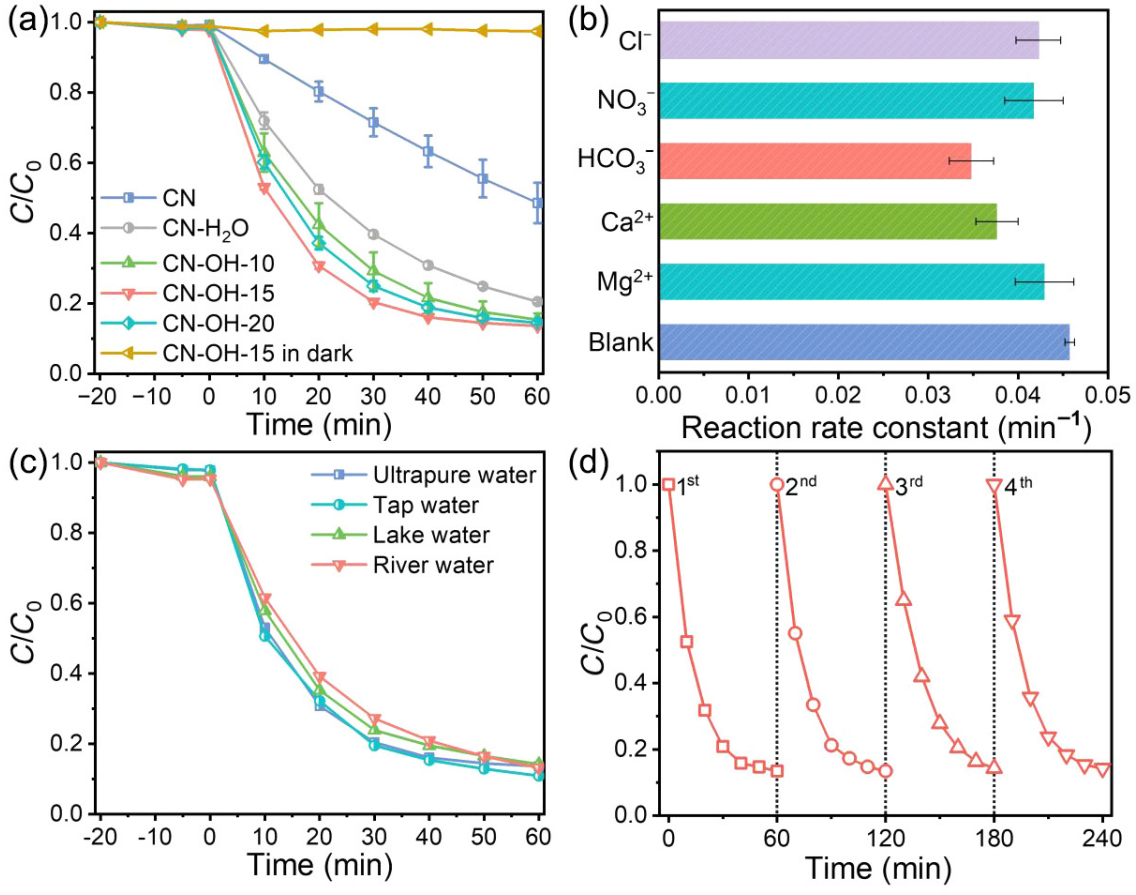

Figure 3 Photocatalytic performance evaluation. (a) Photocatalytic degradation of TC over different catalysts under visible light irradiation. (b) Effect of coexisting anions on TC degradation by CN-OH-15. (c) Photocatalytic degradation of TC over CN-OH-15 in different water matrices. (d) Cycling stability of CN-OH-15 over four consecutive runs.

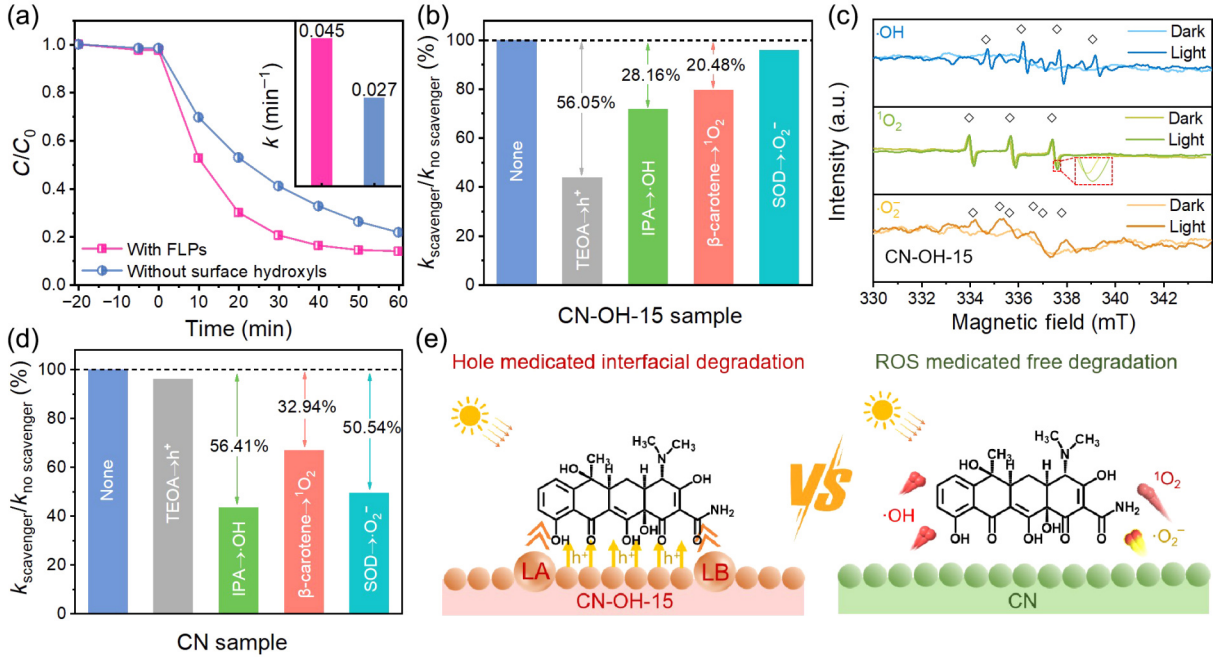

Figure 4 Mechanistic insights into photocatalytic degradation pathways. (a) TC degradation profiles of CN-OH-15 with intact versus thermally disrupted surface hydroxyl groups (inset: corresponding pseudo-first-order rate constants). (b) Effect of radical scavengers on TC degradation over CN-OH-15. (c) EPR spin-trapping spectra confirming ·OH, $^1O_2$, and $\cdot O_2^-$ generation in CN-OH-15. (d) Effect of radical scavengers on TC degradation over pristine CN. (e) Schematic illustration of the hole-mediated interfacial degradation mechanism on CN-OH-15 and the radical-mediated degradation mechanism on pristine CN.

distinctly different pathway, with ROS (including ·OH, $^1O_2$, and $\cdot O_2^-$) acting as the dominant reactive species, while the contribution of photogenerated holes was minimal (Fig. 4(d)). This relied on the stronger ROS generation ability of CN (Fig. S13 in the ESM).

Band gap analyses were conducted to elucidate the origin of this mechanistic difference (Figs. S14 and S15 in the ESM). CN-OH-15 exhibited a more positive valence band maximum (1.89 eV) compared to CN (1.58 eV) and CN-H_2O (1.71 eV) (Fig. S16 and Table S2 in the ESM), reflecting an enhanced oxidative potential of its photogenerated holes. At the same time, the enlarged band gap and weaker reduction potential of CN-OH-15 restricted $\cdot O_2^-$ generation and suppressed exciton dissociation required for $^1O_2$ formation. Taken together, these findings indicate that FLPs enhance photocatalytic activity via a dual mechanism: (1) tuning the valence band to strengthen the oxidative potential of photogenerated holes, and (2) providing effective adsorption sites for TC molecules, which promotes a hole-dominated interfacial oxidation pathway (Fig. 4(e)). In contrast, pristine CN, deficient in such activation sites, operates predominantly via a radical-mediated pathway—a mode inherently less efficient owing to the rapid quenching of ROS in aqueous solutions [7].

3.5 Degradation mechanism and toxicity assessment

In-situ DRIFTS measurements were employed to dynamically probe the FLP-mediated photocatalytic reaction pathway. In these spectra, negative bands indicate the depletion of reactants, whereas positive bands reflect the accumulation of intermediate or product species. During the simulated adsorption stage (Fig. 5(a) and Table S3 in the ESM), the emergence of sharp positive bands at 3650 and 3702–3726 cm^{-1}, corresponding to N–H stretching and free O–H groups, respectively, indicates strong hydrogen-bonding interactions between the surface hydroxyls of CN-OH-15 and TC molecules. Additionally, the intensified absorptions in the 1200–1500 cm^{-1} range, assigned to C–N heterocyclic vibrations, indicate preferential anchoring of TC at CV sites. Upon photocatalytic activation (Fig. 5(b) and Table S3 in the ESM), a gradual depletion of the 3425 cm^{-1} band, attributable to surface hydroxyls, confirms their direct involvement in TC degradation. Concurrently, the negative bands associated with C=O stretching (1775 cm^{-1}), C–H bending (1330 cm^{-1}), and C–N stretching (1126, 1020 cm^{-1}) reveal successive decarbonylation, demethylation, and deamination steps. Meanwhile, the emergence of positive bands in the 1418–1496 cm^{-1} region, assigned to C=C stretching vibrations of aromatic structures, provided strong evidence of progressive oxidative ring-opening reactions, ultimately driving the mineralization of TC's carbon skeleton.

These findings were further corroborated by *in-situ* Raman spectroscopy (Fig. 5(c)). The Raman peaks at 750 and 980 cm^{-1}, corresponding to edge CVs and surface hydroxyls of CN-OH-15, respectively, displayed pronounced attenuation after dark adsorption equilibrium. This observation confirms that FLPs actively participate in anchoring TC molecules at the catalyst surface. As the reaction progressed, the gradual reappearance of the Raman peaks associated with CVs and surface hydroxyls indicates the dynamic desorption of fragmented species from the active sites. This process effectively regenerates the FLPs *in-situ*, which is a key factor contributing to the excellent cycling stability of CN-OH-15. Meanwhile, the characteristic Raman features of TC, including C=O stretching vibrations (1630 cm^{-1}), C–O/C–N stretching (1320 cm^{-1}), C–C skeletal vibrations (930–1140 cm^{-1}), and methyl bending (1436 cm^{-1}) [29, 39], exhibited marked decreases in intensity during visible-light irradiation. These spectral changes provide direct compelling evidence of progressive demethylation and decarbonylation, in excellent agreement with the DRIFTS analysis.

Considering that the hydroxyl and amide groups attached to the aromatic rings impart strong electron-donating characteristics to TC (Fig. S17 in the ESM), the molecules display enhanced affinity for adsorption on CN-OH-15, consistent with its more negative surface potential (Fig. S18 in the ESM). The abundant FLPs in CN-OH-15 exert a pronounced electron "push–pull" effect that plays a central role in TC activation. As illustrated in Fig. 5(d), the LB sites (surface hydroxyls with lone-pair electrons) push electrons into the adsorbed TC molecule, while the LA sites (CVs with an empty

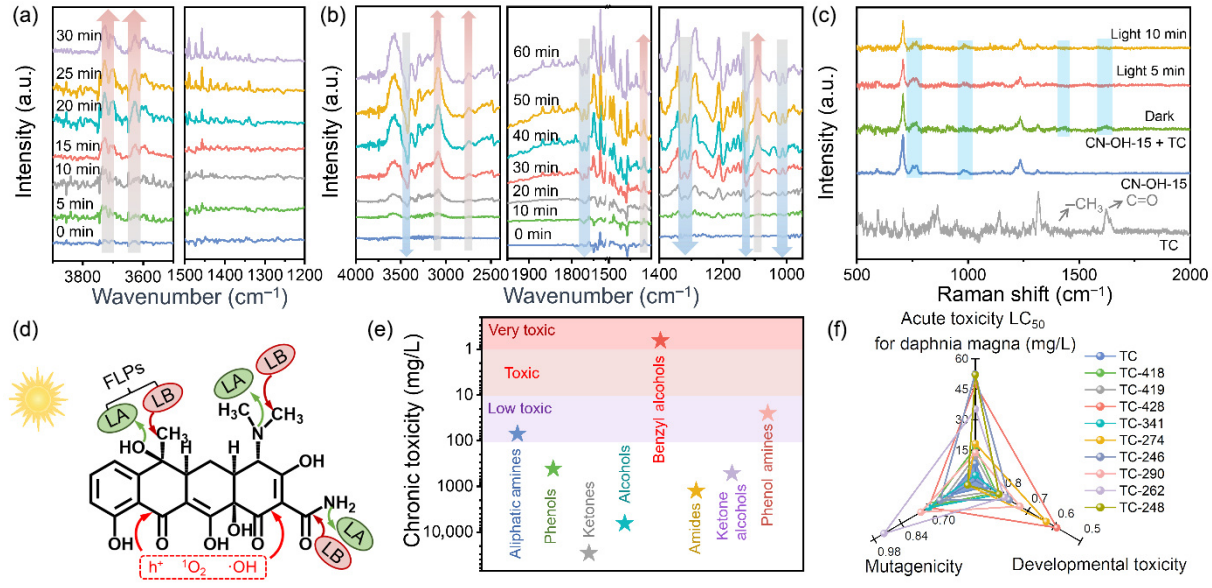

Figure 5 Mechanistic investigation of TC degradation and toxicity assessment. *In-situ* DRIFTS spectra on CN-OH-15 of (a) TC adsorption and (b) TC degradation. (c) *In-situ* Raman spectra of CN-OH-15 during photocatalytic TC degradation. (d) Proposed pathway for TC degradation on CN-OH-15. (e) ECOSAR-based toxicity assessment of key functional groups in TC. (f) Predicted toxicity of degradation intermediates using T.E.S.T.

orbital) pull electrons from it. This synergistic dual-site activation results in efficient polarization of TC molecules, thereby weakening key chemical bonds and predisposing them to oxidative attack. Under visible-light irradiation, these polarized intermediates undergo successive decarbonylation, demethylation, deamination, and aromatic ring-opening reactions, driven by photogenerated holes and supplemented by minor ROS contributions, ultimately leading to complete mineralization.

Subsequently, the intermediate products of TC degradation were systematically identified by HPLC-MS, enabling the construction of detailed degradation pathways (Fig. S19 in the ESM). Initially, the FLP-activated N-methyl groups of TC underwent progressive demethylation under the synergistic action of photogenerated holes and ROS, generating TC-418 and TC-419 intermediates. In a parallel route, ·OH-mediated demethylation triggered rapid dehydration and condensation, yielding the TC-428 intermediate. These intermediates then underwent stepwise structural modifications, including deamidation and dehydroxylation, leading to the formation of TC-341. Concurrently, ring cleavage reactions, accompanied by decarbonization and deamination, produced smaller intermediates such as TC-274, TC-246, and TC-290. Finally, these degradation products were further oxidized and fragmented into low-molecular-weight species, including TC-262 and TC-248, marking advanced breakdown of the tetracycline framework.

The biotoxicity of TC functional groups and degradation intermediates was systematically evaluated using the ECOSAR program, which applies (QSAR) modeling for toxicity prediction. The chronic toxicity of TC molecules toward *Daphnia magna* was found to primarily arise from electron-donating groups, such as benzyl alcohols and amines (Fig. 5(e)). The FLP's synergistic "push-pull" electron effect preferentially activates the electron-donating functional groups that are primarily responsible for TC's toxicity. This targeted activation directs the initial degradation steps toward selective demethylation, deamination, and dehydroxylation, effectively dismantling the toxicophores and leading to the formation of less toxic intermediates, rather than generating random, potentially more harmful by-products. To further assess environmental safety, we performed toxicological prediction of the identified intermediates (Fig. 5(f)). Compared to the parent TC molecule, the intermediates exhibited markedly reduced biotoxicity, developmental toxicity and mutagenicity. These results clearly demonstrate that FLP-mediated photocatalysis not only promotes efficient breakdown of TC but also regulates degradation pathways to suppress the formation of toxic intermediates, thereby ensuring safer end products and enhancing the environmental sustainability of the treatment process.

4 Conclusions

In this study, we successfully synthesized CN catalysts enriched with abundant FLPs for the photocatalytic degradation of TC. The FLPs were constructed through the synergistic pairing of CVs as LA sites and adjacent surface hydroxyls as LB sites. This unique configuration not only promoted efficient charge separation but also enhanced the oxidative potential of photogenerated holes. More importantly, the "push–pull" electronic effect of FLPs enabled effective activation and polarization of TC molecules, thereby facilitating their stepwise degradation. CN-OH-15 catalyst achieved a remarkable photocatalytic degradation rate constant of 0.045 min^{-1}, representing a fourfold enhancement compared to pristine CN. Mechanistic studies revealed that the degradation process predominantly followed a hole-mediated interfacial oxidation pathway, involving sequential demethylation, decarbonylation and ring-opening reactions. The resulting intermediates were either non-toxic or significantly less toxic than the parent TC, which greatly enhanced wastewater biodegradability and facilitated downstream treatment. This work demonstrates that FLP engineering is a powerful and generalizable strategy for designing high-performance photocatalytic systems, showing great promise for the efficient and environmentally friendly remediation of antibiotic-contaminated wastewater in practical scenarios.

Electronic Supplementary Material: Supplementary material (further details of characterizations, band gap analyses, and degradation pathways) is available in the online version of this article at https://doi.org/10.26599/NR.2026.94908399.

Data availability

All data needed to support the conclusions in the paper are presented in the manuscript and the Electronic Supplementary Material. Additional data related to this paper may be requested from the corresponding author upon request.

Acknowledgements

This work was financially supported by the National Natural Science Foundation of China (Nos. 22406144, 42277485, and 22208251), the Department of Science and Technology of Hubei Province (No. 2021CFA034), and State Key Laboratory of Pulp and Paper Engineering (202301). S. A.C. C. acknowledges FCT/MCTES (Fundação para a Ciência e Tecnologia and Ministério da Ciência, Tecnologia e Ensino Superior) for UID/50006/2023 from LAQV and DOI: 10.54499/CEECINST/00102/2018/CP1567/CT0026. We thank the Analytical and Testing Centre of Wuhan Textile University for LC-MS test.

Declaration of competing interest

All the contributing authors report no conflict of interests in this work.

Author contribution statement

Y. X., L. L. M. and Y. S. C.: Data curation, validation and experimental design. X. X.: Conceptualization, data curation, funding acquisition and writing – review & editing. J. J. Z. and S. A.C. C.: Supervision, writing – review & editing, funding acquisition. Z. Y. S., S. W., Z. Y. H., and Y. L. Y.: Data curation, software, investigation. All the authors have approved the final manuscript.

Use of AI statement

None.

References

[1] Zhang, K. F.; Chen, H. X.; Pei, W. B.; Dai, H. X.; Li, J. S.; Zhu, Y. F. Enhanced photocatalytic performance of $Bi_4O_5Br_2$ with three-

dimensionally ordered macroporous structure for phenol removal. *Nano Res.* **2023**, *16*, 8871–8881.
[2] Zhang, N. Q.; Ye, C. L.; Yan, H.; Li, L. C.; He, H.; Wang, D. S.; Li, Y. D. Single-atom site catalysts for environmental catalysis. *Nano Res.* **2020**, *13*, 3165–3182.
[3] Zhu, K.; Wang, L. G.; Hu, Z. F.; Liang, X. Y.; Zhuang, Z. C.; Li, X.; Yang, J. R.; Qiu, R. L.; Wang, D. S.; Yan, K. Curved interface-induced Jahn-teller effect in single-atom catalysts for water purification. *Nat. Commun.* **2025**, *16*, 11047.
[4] Zhang, S. J.; Zheng, H. C.; Tratnyek, P. G. Advanced redox processes for sustainable water treatment. *Nat. Water* **2023**, *1*, 666–681.
[5] Wang, K. Y.; Dai, J.; Zhan, G. M.; Zhao, L.; Wang, R. Z.; Zou, X. Y.; Wang, J. X.; Zheng, Q.; Zhou, B.; Zhao, R. et al. Superior singlet oxygen electrosynthesis via neighboring dual molecular oxygen coactivation for selective tetracycline detoxification. *Angew. Chem., Int. Ed.* **2024**, *63*, e202412209.
[6] Dance, A. Five ways science is tackling the antibiotic resistance crisis. *Nature* **2024**, *632*, 494–496.
[7] Zhang, J. J.; Zhao, Y.; Qi, K. Z.; Liu, S. Y. $CuInS_2$ quantum-dot-modified g-C_3N_4 S-scheme heterojunction photocatalyst for hydrogen production and tetracycline degradation. *J. Mater. Sci. Technol.* **2024**, *172*, 145–155.
[8] Hu, X. L.; Zhang, Z.; Lu, P.; Zhou, Y. H.; Zhou, Y. Y.; Bai, Y.; Yao, J. J. Cyano-deficient g-C_3N_4 for round-the-clock photocatalytic degradation of tetracycline: Mechanism and application prospect evaluation. *Water Res.* **2024**, *260*, 121936.
[9] Shen, H. D.; Zhan, X. Y.; Hong, S.; Xu, L.; Yang, C. M.; Robertson, A. W.; Hao, L. D.; Fu, F.; Sun, Z. Y. Ultrafine MoO_x clusters anchored on g-C_3N_4 with nitrogen/oxygen dual defects for synergistic efficient O_2 activation and tetracycline photodegradation. *Nano Res.* **2023**, *16*, 10713–10723.
[10] Liu, X.; Sau, A.; Green, A. R.; Popescu, M. V.; Pompetti, N. F.; Li, Y. Z.; Zhao, Y. C.; Paton, R. S.; Damrauer, N. H.; Miyake, G. M. Photocatalytic C–F bond activation in small molecules and polyfluoroalkyl substances. *Nature* **2025**, *637*, 601–607.
[11] He, X. H.; Kai, T.; Ding, P. Heterojunction photocatalysts for degradation of the tetracycline antibiotic: A review. *Environ. Chem. Lett.* **2021**, *19*, 4563–4601.
[12] Zhang, W. X.; Luo, Y.; Carabineiro, S. A. C.; Lyu, S.; Xiao, W. W.; He, Z. Y.; Zheng, Z.; Zhu, J. J. Stabilizing Co nanoparticles for CO_2 hydrogenation by lattice-matching confinement in ZnO interlayers. *Nano Res.* **2025**, *18*, 94907282.
[13] Xu, X.; Cui, Y. Y.; Chen, T.; Jiang, K.; Wang, J.; Xiao, Y.; Yang, X. L.; Zhu, J. J.; Chen, H.; Ding, X. Dual-site synergetic photochemical activation of chlorinated phenols triggered by surface hydroxyls of photocatalysts under visible light. *ACS Catal.* **2023**, *13*, 4700–4710.
[14] Gu, X. Y.; Lin, S.; Qi, K. Z.; Yan, Y.; Li, R. C.; Popkov, V.; Almjasheva, O. Application of tungsten oxide and its composites in photocatalysis. *Sep. Purif. Technol.* **2024**, *345*, 127299.
[15] Xu, X.; Ding, X.; Yang, X. L.; Wang, P.; Li, S.; Lu, Z. X.; Chen, H. Oxygen vacancy boosted photocatalytic decomposition of ciprofloxacin over Bi_2MoO_6: Oxygen vacancy engineering, biotoxicity evaluation and mechanism study. *J. Hazard. Mater.* **2019**, *364*, 691–699.
[16] Yang, X. L.; Wang, S. Y.; Chen, T.; Yang, N.; Jiang, K.; Wang, P.; Li, S.; Ding, X.; Chen, H. Chloridion-induced dual tunable fabrication of oxygen-deficient Bi_2WO_6 atomic layers for deep oxidation of NO. *Chin. J. Catal.* **2021**, *42*, 1013–1023.
[17] Zhou, B.; Yu, L. H.; Zhang, W. X.; Liu, X. P.; Zhang, H.; Cheng, J. D.; Chen, Z. Y.; Zhang, H.; Li, M. Q.; Shi, Y. B. et al. Cu_1−Fe dual sites for superior neutral ammonia electrosynthesis from nitrate. *Angew. Chem., Int. Ed.* **2024**, *63*, e202406046.
[18] Wang, B. W.; Zhang, N.; Xiao, P.; Zhang, J.; Carabineiro, S. A. C.; Zhu, J. J. Carbon coated $LaFe_{0.92}Pd_{0.08}O_3$ composites for catalytic transfer hydrogenation: Balance in the ability of substrates adsorption and conversion. *Nano Res.* **2024**, *17*, 3724–3732.
[19] Ye, X. H.; Li, Y.; Luo, P. P.; He, B. C.; Cao, X. X.; Lu, T. B. Iron sites on defective BiOBr nanosheets: Tailoring the molecular oxygen activation for enhanced photocatalytic organic synthesis. *Nano Res.* **2022**, *15*, 1509–1516.
[20] Su, Y. T.; Han, B. W.; Meng, Q. J.; Luo, X. Q.; Wu, Z. B.; Weng, X. L. Unveiling the function of oxygen vacancy on facet-dependent CeO_2 for the catalytic destruction of monochloromethane: Guidance for industrial catalyst design. *Environ. Sci. Technol.* **2024**, *58*, 8086–8095.
[21] Li, J. S.; Li, G. C.; Tsang, S. C. E. Heterogeneous frustrated Lewis pair catalysts: Rational structure design and mechanistic elucidation based on intrinsic properties of supports. *Acc. Chem. Res.* **2025**, *58*, 555–569.
[22] Peng, J. C.; Dong, D. D.; Wang, Z. Y.; Yang, H.; Qiao, D. Y.; Wang, Q. Q.; Sun, W.; Liu, M. M.; Wang, J. J.; Zhu, M. Y. et al. Manipulating micro-electric field and coordination-saturated site configuration boosted activity and safety of frustrated single-atom Cu/O Lewis pair for acetylene hydrochlorination. *Nano Res.* **2023**, *16*, 9039–9049.
[23] Liu, K. S.; Liu, T. T.; Wu, X. Y.; Dai, J.; Chen, Q. J.; Wan, J.; Liu, L. Frustrated Lewis pair chemistry in 2D CeO_2 for efficient alkaline hydrogen evolution. *J. Mater. Chem. A* **2024**, *12*, 28843–28852.
[24] Zou, Y. J.; Mao, C. L.; Xu, M. K.; Xing, C.; Wang, R. Z.; Ozin, G. A.; Ling, L. Surface frustrated Lewis pairs in titanium nitride enable gas phase heterogeneous CO_2 photocatalysis. *Nat. Commun.* **2024**, *15*, 10604.
[25] Yang, J.; Xiong, S. F.; Hao, J.; Yang, H. Y.; Guo, X. P.; Xiao, X. S.; Shen, Z. G. Construction of dual vacancies and frustrated Lewis pairs-modified Bi_2WO_6 nanosheets for efficient photocatalytic conversion of CO_2 to CO. *J. Catal.* **2024**, *437*, 115665.
[26] Song, J. X.; Zhu, P. F.; Ma, W. M.; Sun, N.; Li, Y. X. Boosting photocatalytic CO_2 reduction with H_2O by oxygen vacancy- and hydroxyl-tailored $SrBi_2Ta_2O_9$ surface-frustrated Lewis pairs. *ACS Catal.* **2023**, *13*, 12700–12710.
[27] Yue, Y. X.; Zuo, F. M.; Wang, B. L.; Xian, X. L.; Tang, J.; Zhang, H. F.; Zhang, Z. L.; Ke, Q. P.; Chen, W. Highly efficient catalyst for 1,1,2-trichloroethane dehydrochlorination via BN_3 frustrated Lewis acid-base pairs. *Nano Res.* **2024**, *17*, 4773–4781.
[28] Li, Z.; Mao, C. L.; Pei, Q. J.; Duchesne, P. N.; He, T.; Xia, M. K.; Wang, J. T.; Wang, L.; Song, R.; Ali, F. M. et al. Engineered disorder in CO_2 photocatalysis. *Nat. Commun.* **2022**, *13*, 7205.
[29] Yu, L. Q.; Wang, Q. S.; Zhuang, C. Q.; Huang, J. D.; Zhu, Y. A.; Jing, X. D.; Guo, Y. H.; Tong, Y. X.; Zhang, Z. Y. Periodic frustrated Lewis pairs on bimetallic oxide semiconductors for CO_2 adsorption and photocatalytic conversion. *ACS Nano* **2025**, *19*, 7239–7252.
[30] Ban, T.; Yu, X. Y.; Kang, H. Z.; Huang, Z. Q.; Li, J.; Chang, C. R. Design of SA-FLP dual active sites for nonoxidative coupling of methane. *ACS Catal.* **2023**, *13*, 1299–1309.
[31] Pu, W. J.; Zhou, Y. Q.; Yang, L. F.; Gong, H. F.; Li, Y. H.; Yang, Q. Y.; Zhang, D. Q. High-efficiency crystalline carbon nitride photocatalysts: Status and perspectives. *Nano Res.* **2024**, *17*, 7840–7863.
[32] Xu, X.; Xiao, Y.; Xu, X. L.; Carabineiro, S. A. C.; Zhu, J. J. Dual-site engineering of N vacancies and K single-atoms in C_3N_4: Enabling spatial charge transfer channels for photocatalysis. *J. Materiomics* **2025**, *11*, 100969.
[33] Ma, L. X.; Gao, Y. P.; Wei, B. Q.; Huang, L.; Zhang, N.; Weng, Q.; Zhang, L.; Liu, S. F.; Jiang, R. B. Visible-light photocatalytic H_2O_2

production boosted by frustrated Lewis pairs in defected polymeric carbon nitride nanosheets. *ACS Catal.* **2024**, *14*, 2775–2786.

[34] Shang, Y. R.; Zheng, M.; Liu, H. J.; Jin, X. L.; Yan, C. S.; Song, L.; Qi, Z. M.; Jing, F. Y.; Song, P.; Zhou, X. et al. Mimicking frustrated Lewis pairs on graphitic carbon nitride for CO_2 photoreduction. *ACS Catal.* **2023**, *13*, 14530–14539.

[35] Yu, M. J.; Lin, H. G.; Zhang, Y. C.; Shu, W. Y.; Wu, G. Y.; Xing, W. N. Frustrated Lewis pairs on hollow flower-liked carbon nitride by phosphorous and tungsten co-doping to enhance photocatalytic performance. *J. Mol. Struct.* **2025**, *1319*, 139510.

[36] Yang, X. L.; Cheng, L.; Zhang, Q.; Yu, L.; Qi, X.; Mao, J.; Li, P. W. Insight into the boosted ZEN degradation over defective Bi_2WO_6 ultrathin layers: ROS-mediated mechanism and application in corn oil. *Food Chem.* **2023**, *405*, 134895.

[37] Xu, X.; Wang, J.; Chen, T.; Yang, N.; Wang, S. Y.; Ding, X.; Chen, H. Deep insight into ROS mediated direct and hydroxylated dichlorination process for efficient photocatalytic sodium pentachlorophenate mineralization. *Appl. Catal. B: Environ.* **2021**, *296*, 120352.

[38] Li, Y. H.; Ren, Z. T.; He, Z. J.; Ouyang, P.; Duan, Y. Y.; Zhang, W. D.; Lv, K. L.; Dong, F. Crystallinity-defect matching relationship of g-C_3N_4: Experimental and theoretical perspectives. *Green Energy Environ.* **2024**, *9*, 623–658.

[39] Wang, Y.; Li, L. X.; Zhou, P. Y.; Gan, Y.; Liu, W. P.; Wang, Y. W.; Deng, Y. L.; Li, H. P.; Xie, M.; Xu, Y. G. Aeration-free photo-Fenton-like reaction mediated by heterojunction photocatalyst toward efficient degradation of organic pollutants. *Angew. Chem., Int. Ed.* **2025**, *64*, e202419680.